PWM Resonant Converter With Asymmetric Modulation for ZVS Active Voltage Doubler Rectifier and Forced Half Resonance in PV Application

Jong-Woo Kim, *Member, IEEE*, Moo-Hyun Park, *Student Member, IEEE*,
Jung-Kyu Han, *Student Member, IEEE*, Moonhyun Lee, *Student Member, IEEE*,
and Jih-Sheng Lai, *Life Fellow, IEEE*

***Abstract*—In photovoltaic applications, many previous research works have focused on pulsewidth modulation (PWM) resonant converters in order to achieve a high efficiency with a wide input voltage range. Conventional approaches utilized symmetric boosting modulation at the secondary side rectifier to obtain a symmetric operation, and they utilized two boosting modes in a switching period. Among various rectifier structures, the voltage doubler structure has a strong advantage due to a small number of components. However, it suffers from serious hard switching losses in the secondary side rectifier. In this paper, a new converter with a novel asymmetrical modulation is proposed and verified. The strong point of the proposed converter is that it eliminates hard switching turn-ON losses from the rectifier, while maintaining the minimized number of components. Although the proposed converter adopts an asymmetric modulation, the offset current on the transformer becomes zero inherently. Furthermore, a "forced half resonance" operation of the proposed converter keeps rms current stresses at the same level as conventional converter although it has a higher peak current. Accordingly, the proposed converter achieves a superior efficiency with the minimum number of components at 35–25 V input and 380 V/300 W output specification.**

***Index Terms*—DC–DC power conversion, photovoltaic, resonant power conversion.**

I. INTRODUCTION

PHOTOVOLTAIC (PV) is one of the most promising renewable energy sources [1]–[3] due to its powerful advantages such as easy installation with small space, silence, and low maintenance cost. The requirement for power converters in PV applications is a high step-up capability and high efficiency with a wide input voltage and power range.

Conventional high step-up converters are based on a boost converter [4]–[12] or a series resonant converter [13]–[26]. The boost converter based approaches combine coupled inductor or/and switched capacitor with a conventional boost converter to achieve a high step-up voltage conversion ratio. These methods stack several voltage boosting cells in order to achieve a high step-up voltage conversion ratio. However, this means there exist a large number of power conversion stages in one step-up converter, resulting in the limitation on the efficiency. Most importantly, these boost converter based approaches usually fail to achieve zero voltage switching (ZVS) of the main switch, further limiting the efficiency.

For these reasons, step up resonant converters can be strong candidates in PV application since they have a small number of components and high efficiency due to inherent soft switching characteristics. Among various resonant converter topologies, an *LLC* converter is widely used in the industry [27]–[33] because it has a simple structure and wider voltage gain capability with pulse-frequency modulation. However, many researchers pointed out the disadvantage of an *LLC* converter in applications where a wide voltage gain is required [27]–[33]. In order to cover a wide gain, an *LLC* resonant converter should be designed with a small ratio of the magnetizing inductance to the resonant inductance. This results in a large circulating loss in the primary side and also large turn-OFF losses of switching components.

In order to obtain a higher efficiency with wide input voltage range, many researchers have focused on pulsewidth modulation (PWM) applied resonant converters [13]–[26]. PWM resonant converters operate at a constant switching frequency and regulate output voltage using a duty ratio of an active bridge cell. The active bridge cell to obtain a wide conversion ratio can be buck or boost type, and can be placed at the primary side or the secondary side of the converter. The key concept of PWM controlled resonant converters is to obtain a buck or boost converter operation in a resonant converter. Regardless of the position of the active bridge cell, they buck or boost the resonant inductor current according to the duty cycle of the active bridge cell. In PV application, it is relatively advantageous to have the boosting cell at the secondary side due to a large current at the primary side due to a high step-up conversion ratio. When the active bridge

---

Manuscript received December 11, 2018; revised March 6, 2019; accepted April 19, 2019. Date of publication April 28, 2019; date of current version October 18, 2019. Recommended for publication by Associate Editor D. O. Neacsu. *(Corresponding author: Jong-Woo Kim.)*

J.-W. Kim, M. Lee, and J.-S. Lai are with the Future Energy Electronics Center, Bradley Department of Electrical and Computer Engineering, Virginia Tech, Blacksburg, VA 24061 USA (e-mail: kimjw@vt.edu; leemh@vt.edu; laijs@vt.edu).

M.-H. Park and J.-K. Han are with the Department of Electrical Engineering, Korea Advanced Institute of Science and Technology, Daejeon 34141, South Korea (e-mail: moohyun3@kaist.ac.kr; hanjk715@kaist.ac.kr).

Color versions of one or more of the figures in this paper are available online at http://ieeexplore.ieee.org.

Digital Object Identifier 10.1109/TPEL.2019.2914016

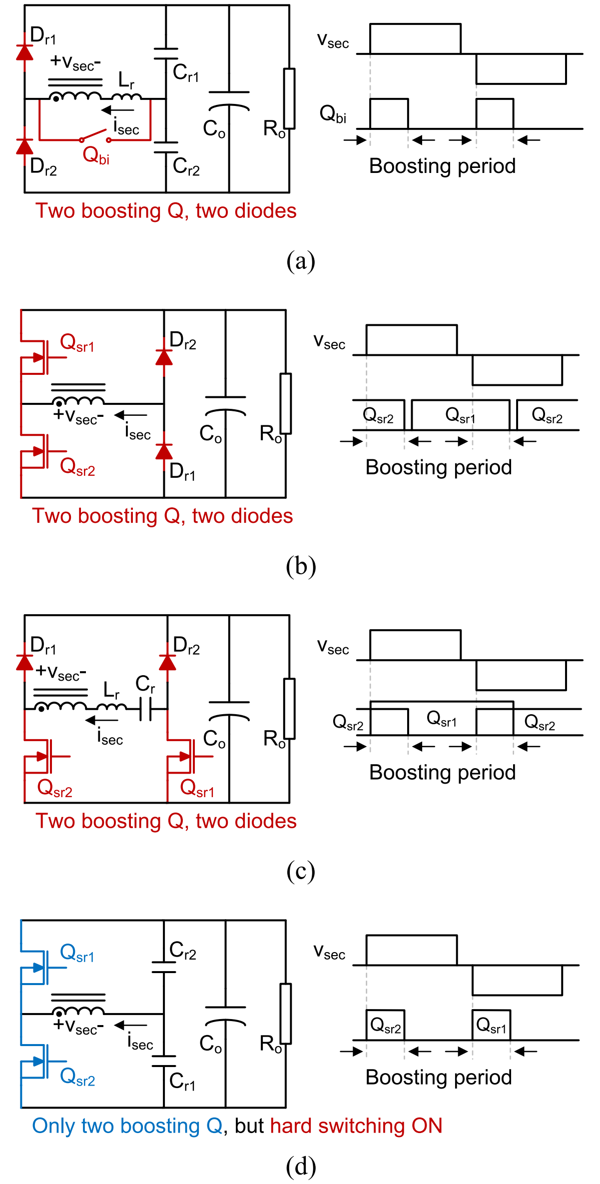

Fig. 1. Secondary side configurations and control schemes of conventional PWM adapted resonant converters. (a) Based on bidirectional switch [16]–[18]. (b) Based on phase shifted gate signal [19]. (c) Based on extended gate signal [20]–[22]. (d) Based on active voltage doubler version [23]–[26].

cell is located at the primary side or a buck type, it suffers from a large turn-OFF switching losses. Therefore, this paper focuses on the PWM applied resonant converters, which have the boosting cell at the secondary side [16]–[26].

The key concept of the PWM applied resonant converters with the secondary side boosting cell is to form a short circuit at the secondary side of the transformer. Fig. 1 represents the secondary side configurations and control schemes of conventional PWM adapted resonant converters. Fig. 1(a) represents the bidirectional switch based method [16]–[18] and its gate signal. Bidirectional switch $Q_{\rm bi}$ was formed by two MOSFETs, so the usage of $Q_{\rm bi}$ is inefficient since it is used only in a boost mode. Furthermore, $Q_{\rm bi}$ is hard switching device. Fig. 1(b) and (c) represents phase shifted [19] and symmetrically extended gate signal methods [20]–[22]. These two methods are more attractive compared to the bidirectional switch methods, because they just replaced rectifier diodes to synchronous rectifiers Q_{sr1} and Q_{sr2}. Q_{sr1} and Q_{sr2} provide the boost operation and also synchronous rectification, so that they can reduce conduction losses in the secondary side rectifiers. However, they still need a large number of components in the secondary side; two switches and two diodes.

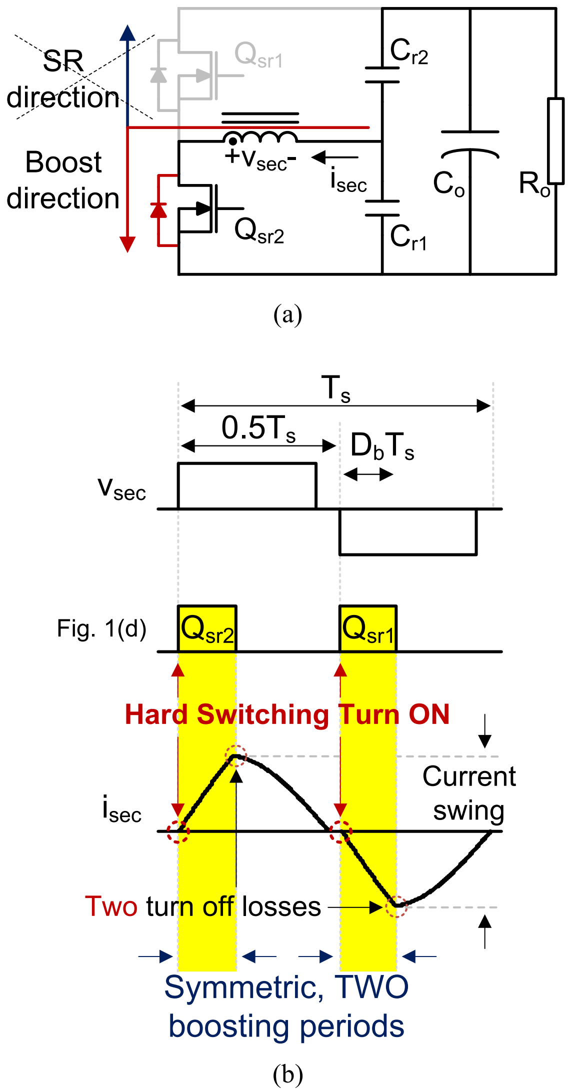

Fig. 2. Limitation of conventional active voltage doubler rectifier [23]–[26]: large switching turn-ON losses. (a) Current path during the boost period. (b) Conceptual waveforms.

Fig. 1(d) represents a PWM resonant converter employing active voltage doubler recitifier [23]–[26]. The advantage of this configuration is the small number of components in the rectifier, in that it utilizes only two switching components. Due to the cost effectiveness, the most recent studies focused on the active voltage doubler rectifier. However, as shown in Fig. 2, the active rectifier switches are suffering from hard switching turn-ON losses, and the switching loss severely affects the efficiency in a boost mode.

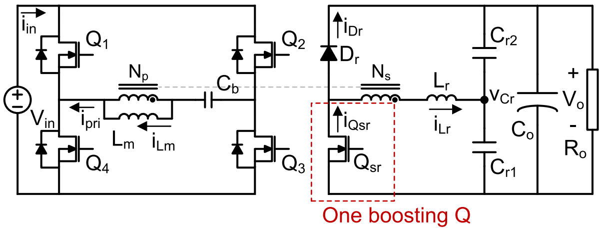

Fig. 3. Proposed converter: only one boosting switch utilized for the active voltage doubler rectifier.

Fig. 2 represents the reason of hard switching in the conventional active voltage doubler rectifier. Fig. 2(a) represents the current path of the conventional active voltage doubler rectifier during the boosting period. When the active switches are utilized as the synchronous rectifiers to reduce the conduction losses, Q_{sr1} is turned ON when the secondary side transformer voltage v_{sec} is positive. The switch is turned ON after the voltage across Q_{sr1} decreases to zero by the resonant current, ZVS is naturally obtained. However, in PWM resonant converters, the active rectifier turns ON Q_{sr2} when v_{sec} is positive in order to build the resonant current with a large slope. This results in two times of switching energy occurring in a switching period, as shown in Fig. 2(b). Since the hard switching losses always occur when the converter operates in a boost mode, they become a main cause of efficiency decrement especially in a light load condition.

In this paper, a new PWM resonant converter with a novel asymmetrically extended modulation is proposed and verified. The strong point of the proposed converter is that it eliminates hard switching turn-ON losses from the rectifier, while maintaining the minimized number of components. Although the proposed converter adopts an asymmetric modulation, the offset current on the transformer becomes zero inherently. Furthermore, a "forced half resonance" operation of the proposed converter keeps rms current stresses at the same level as conventional converter although it has a higher peak current.

II. Proposed Converter

Fig. 3 represents the proposed converter. The proposed converter utilizes only one boosting switch, whereas conventional methods utilize two boosting switches in the secondary side as mentioned before. It can be note that the offset current of the transformer becomes inherently zero in all conditions, since the average currents through the transformer becomes zero in both the primary and secondary side, according to the charge balance of the blocking capacitor C_b and the resonant capacitors C_{r1} and C_{r2}. This characteristic allows utilizing various kinds of modulation schemes, even including asymmetric modulation.

Fig. 4 represents the gate signals and current waveforms compared to conventional approaches. The primary side switches Q_1/Q_3 and Q_2/Q_4 are turned ON alternatively with 0.5 duty ratio at the resonant frequency. When the input voltage is the maximum, the gate signal for Q_{sr} is identical to that of Q_2/Q_4. The waveforms are abbreviated since it is the same with conventional series resonant converters. In a boost mode, the gate signal for Q_{sr} is extended so that it overlaps the gate signals for Q_1/Q_3 so that the inductor current can be boosted. One of key features of the proposed modulation is that the current waveform is forced to be sinusoidal during the half switching period. This "forced half resonant operation" eliminates one switching turn-OFF loss and also reduces current swings in the overall circuit. Most importantly, it should be noted that Q_{sr} is turned ON as a synchronous rectifier eliminating turn-ON loss of the conventional active voltage doubler rectifier.

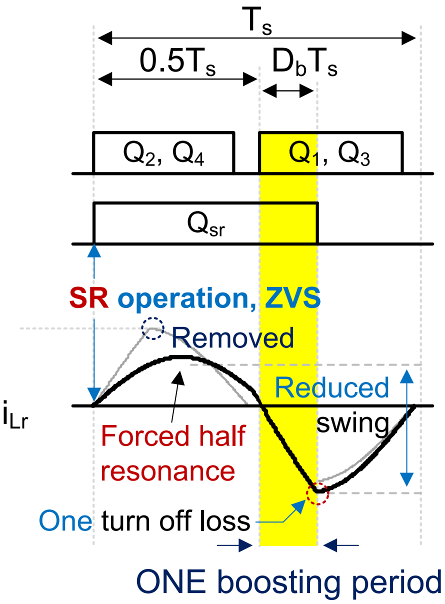

Fig. 4. Gate signals and current waveform comparison of the proposed converter: ZVS due to SR operation, eliminated one turn-OFF loss and reduced current swing due to "forced half resonance."

III. Steady-State Analysis

In order to avoid complexity in the steady-state analysis, some assumptions are made as follows.

1) The switching frequency is constant as the resonant frequency.
2) Turns ratio of the transformer is $N_p{:}N_s = 1 : n$.
3) Magnetizing inductor L_m of the transformer is large enough to neglect the ripple current. It makes the magnetizing current i_{Lm} zero due to the charge balance of the blocking and resonant capacitors (C_b, C_{r1}, and C_{r2} in Fig. 3).
4) Capacitance of the blocking capacitor C_b is large enough to neglect ripple voltage. In this case, the voltage across C_b becomes zero.
5) Deadtime between gate signals are short enough to be neglected.
6) Switching devices are ideal.

A. Operating Mode Analysis

Figs. 5 and 6 illustrate the steady-state waveforms and operating modes and their simplified circuit in a boost mode.

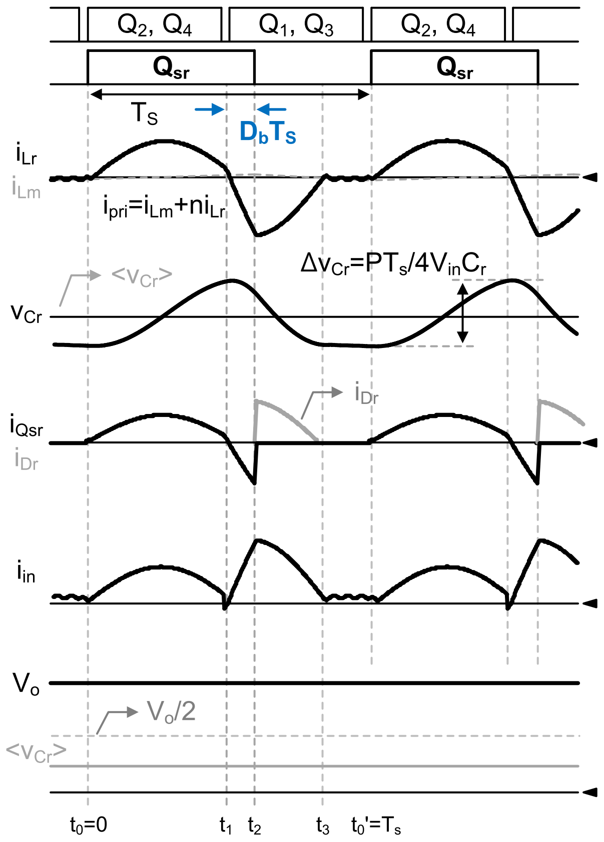

Fig. 5. Key steady-state waveforms in a boost mode.

The operation with a boost mode can be divided into four modes during a switching period. Primary side current i_{pri} is the sum of the magnetizing current i_{Lm} and the resonant inductor current i_{Lr} reflected to the primary side, divided by *n*. By applying the charge balance condition on C_b, it can be noted that the average value of i_{pri} becomes zero. Also, applying the charge balance condition on C_{r1} and C_{r2} leads to the fact that the average value of i_{Lr} is also zero. Therefore, the average value of i_{Lm} becomes also zero, and i_{Lm} becomes zero when ignoring the ripple current. In the following analysis, the resonant inductor current and voltage across C_{r1} at t_n are defined as i_{Lrn} and v_{Crn} for simplicity.

Mode 1 ($t_0 = 0 - t_1 = T_s/2$) begins when Q_2, Q_4, and Q_{sr} are turned ON. i_{Lr} resonates according to the resonance of the resonant inductor L_r and resonant capacitor C_r. i_{Lr0} is zero. It is assumed that the current of the magnetizing inductor i_{Lm} is zero as mentioned before. Therefore, the simplified circuit forms a simple *LC* resonant circuit. In mode 1, state equations can be expressed as follows:

$$Zi_{Lr}(t) = (nV_{\text{in}} - (< v_{Cr} > + v_{Cr0}))\sin(\omega t) \qquad (1)$$

$$\begin{aligned} v_{Cr}(t) = {} & (nV_{\text{in}} - < v_{Cr} >) \\ & - (nV_{\text{in}} - (< v_{Cr} > + v_{Cr0}))\cos(\omega t) \end{aligned} \qquad (2)$$

where V_{in}, ω, Z, v_{Cr}, and $< v_{Cr} >$ represent the input voltage, $1/\sqrt{L_rC_r} = 1/\sqrt{L_r(C_{r1}+C_{r2})}$, $\sqrt{L_r/C_r}$, voltage ON C_{r1}, and the average value of v_{Cr}, respectively. Combining (1) and (2) leads to the state trajectory equation as follows:

$$\begin{aligned} & [v_{Cr} - (nV_{\text{in}} - < v_{Cr} >)]^2 + [Zi_{Lr}]^2 \\ & = [nV_{\text{in}} - (< v_{Cr} > + v_{Cr0})]^2. \end{aligned} \qquad (3)$$

From (3), it can be noted that the state trajectory of v_{Cr} and Zi_{Lr} forms a circle whose center C_1 and radius R_1 are $(nV_{\text{in}} - < v_{Cr} >, 0)$ and $nV_{\text{in}} - (< v_{Cr} > + v_{Cr0})$. Mode 1 ends when Q_2 and Q_4 are turned OFF. The duration of mode 1 is a half resonant period so that mode 2 begins with zero current.

Mode 2 (t_1–t_2) begins when Q_1 and Q_3 are turned ON. Since Q_{sr} is still turned ON, i_{Lr} is boosted. The only difference between modes 1 and 2 is the direction of V_{in}/n as shown in Fig. 6(b). According to the simplified circuit for mode 2, the state and their trajectory equations can be expressed as follows:

$$Zi_{Lr}(t - t_1) = -(nV_{\text{in}} + < v_{Cr} > + v_{Cr1})\sin(\omega(t - t_1)) \qquad (4)$$

$$\begin{aligned} v_{Cr}(t) = {} & -(nV_{\text{in}} + < v_{Cr} >) \\ & - (nV_{\text{in}} + < v_{Cr} > + v_{Cr1})\cos(\omega t) \end{aligned} \qquad (5)$$

$$\begin{aligned} & [v_{Cr} + nV_{\text{in}} + < v_{Cr} >]^2 + [Zi_{Lr}]^2 \\ & = [nV_{\text{in}} + < v_{Cr} > + v_{Cr1}]^2. \end{aligned} \qquad (6)$$

From (6), the state trajectory in mode 2 forms a circle whose center C_2 is $(-nV_{\text{in}} - < v_{Cr} >, 0)$ and radius R_2 is $nV_{\text{in}} + < v_{Cr} > + v_{Cr1}$. Mode 2 ends when Q_{sr} is turned OFF. The duration of mode 2 will be denoted as D_bT_s where D_b and T_s represent boosting duty ratio and switching period, respectively.

Mode 3 (t_2–t_3) begins when the rectifier diode D_r is turned ON after Q_{sr} is turned OFF. The boosted current in mode 2 is delivered to the output side and i_{Lr} decreases. The state and trajectory equations can be expressed as follows:

$$\begin{aligned} & Zi_{Lr}(t - t_2) = Zi_{Lr2}\cos(\omega(t - t_2)) \\ & + [-nV_{\text{in}} - v_{Cr2} + (V_o - < v_{Cr} >)]\sin(\omega(t - t_2)) \end{aligned} \qquad (7)$$

$$\begin{aligned} & v_{Cr}(t - t_2) - [-nV_{\text{in}} + (V_o - < v_{Cr} >)] \\ & = Zi_{Lr2}\sin(\omega(t - t_2)) - [-nV_{\text{in}} - v_{Cr2} \\ & + (V_o - < v_{Cr} >)]\cos(\omega(t - t_2)) \end{aligned} \qquad (8)$$

$$\begin{aligned} & [v_{Cr} - (-nV_{\text{in}} + V_o - < v_{Cr} >)]^2 + [Zi_{Lr}]^2 \\ & = [-nV_{\text{in}} - v_{Cr2} + (V_o - < v_{Cr} >)]^2 + [Zi_{Lr2}]^2. \end{aligned} \qquad (9)$$

From (9), the state trajectory in mode 3 forms a circle whose center C_3 is $(-nV_{\text{in}} + V_o - < v_{Cr} >, 0)$ and radius R_3 is $\sqrt{[-nV_{\text{in}} - v_{Cr2} + (V_o - < v_{Cr} >)]^2 + [Zi_{Lr2}]^2}$. Mode 3 ends when i_{Lr} becomes zero and D_r is turned OFF.

Mode 4 (t_3–t_0') begins when i_{Lr} becomes zero and D_r is turned OFF. Since we assumed that i_{Lm} is zero for all switching period, the states do not vary during mode 4, and the state trajectory stays at the point $(v_{Cr3}, 0)$. Mode 4 ends when Q_1 and Q_3 are turned OFF and the mode goes back to mode 1 after Q_2 and Q_4 are turned ON.

At this point, it can be noted that there is no expense on the voltage conversion ratio although the boosting mode occurs only

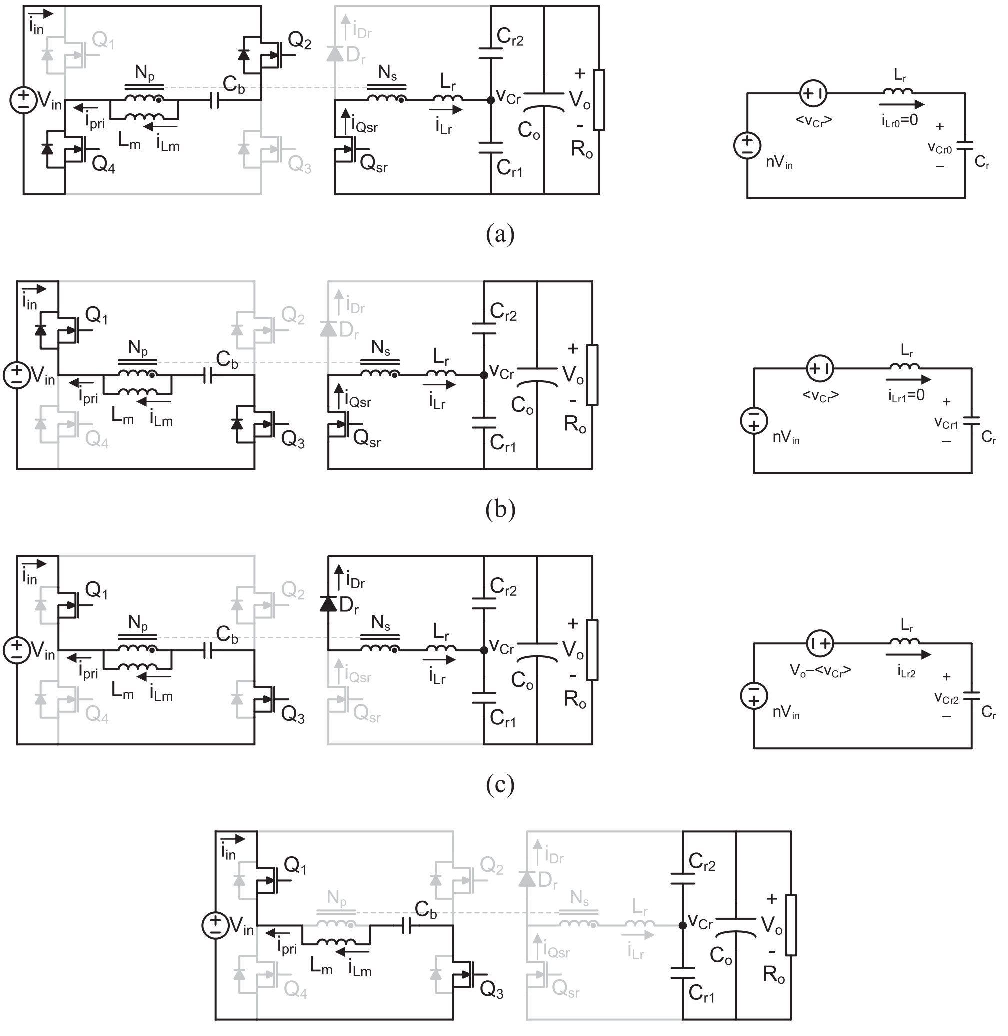

(a)

(b)

(c)

(d)

Fig. 6. Operating modes and their simplified *LC* resonant circuits. (a) In mode 1 (t_0–t_1). (b) In mode 2 (t_1–t_2). (c) In mode 3 (t_2–t_3). (d) In mode 4 (t_3–t_0').

once in the switching period, because the same amount of input power is delivered during the forced half resonant operation as shown in the input current i_{in} waveform in Fig. 5.

B. Required Boosting Duty Ratio According to Operating Condition

The state trajectory presented in Fig. 7 can lead to the required boosting duty ratio with geometric analysis. Required D_b to obtain appropriate V_o can be obtained when the operating conditions such as operating power *P*, *n*, V_{in}, V_o, T_s, L_r, and C_r. From mode analysis, the input power *P* can be expressed as follows:

$$P = V_{\text{in}} I_{\text{in}} = V_{\text{in}} C_r 2n\Delta v_{Cr}/T_s = 4nV_{\text{in}} C_r R_1/T_s \tag{10}$$

where I_{in} and Δv_{Cr} represent the average input current and the ripple on v_{Cr}. Rearranging (10) leads to R_1 as follows:

$$R_1 = \frac{PT_s}{4nV_{\text{in}} C_r}. \tag{11}$$

Distances between O_1 and v_{Cr0}/v_{Cr1} allows to express v_{Cr0} and v_{Cr1} related to the operating conditions as follows:

$$v_{Cr0} = O_{1x} - R_1 = nV_{\text{in}} - < v_{Cr} > -PT_s/4nV_{\text{in}} C_r \tag{12}$$

$$v_{Cr1} = O_{1x} + R_1 = nV_{\text{in}} - < v_{Cr} > +PT_s/4nV_{\text{in}} C_r \tag{13}$$

where O_{1x} represents the x-coordinate value of O_1. From now, O_{nx} represents the x-coordinate value of O_n.

R_2 can be expressed with the operating conditions by obtaining the distance between O_2 and v_{Cr1} as follows:

$$R_2 = v_{Cr1} - O_{2x} = 2nV_{\text{in}} + PT_s/4nV_{\text{in}} C_r \tag{14}$$

v_{Cr2} can be expressed with the operating conditions and the boosting duty ratio D_b as follows:

$$\begin{aligned} v_{Cr2} &= O_{2x} + R_2 \cos(\omega D_b T_s) \\ &= -nV_{\text{in}} - < v_{Cr} > +R_2 \cos(\omega D_b T_s). \end{aligned} \tag{15}$$

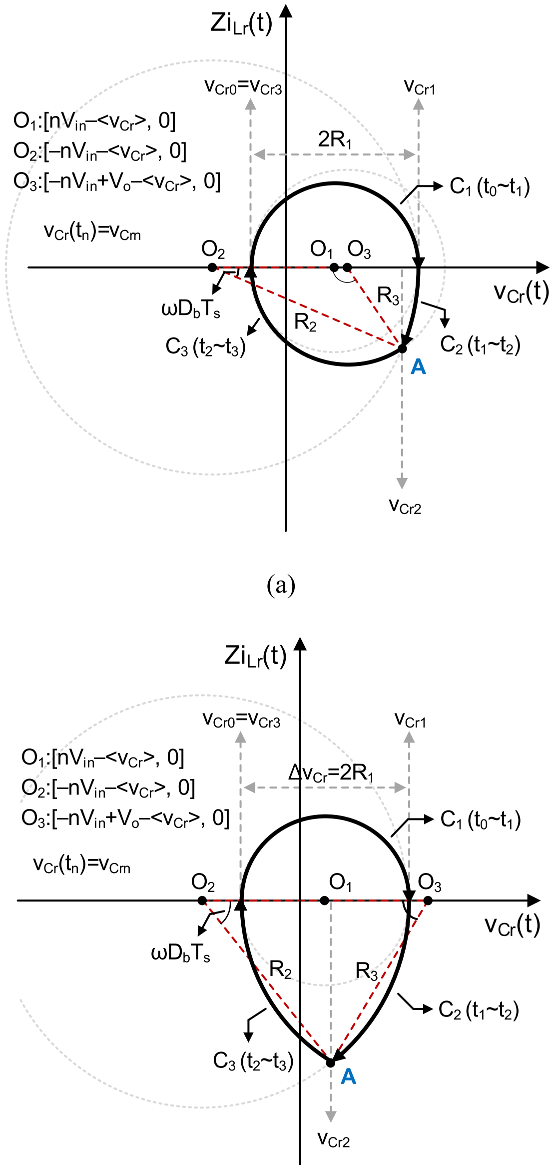

(a)

(b)

Fig. 7. State trajectory. (a) In shallow boost region ($\angle O_2O_3A > 90°$). (b) In deep boost region ($\angle O_2O_3A < 90°$).

R_3 can be expressed as follows:

$$\begin{aligned} R_3 &= O_{3x} - O_{2x} - [(O_{1x} - O_{2x}) - R_1] \\ &= V_o - 2nV_{\text{in}} + PT_s/4nV_{\text{in}}C_r. \end{aligned} \tag{16}$$

Finally, applying the cosine law to the triangle O_2O_3A allows obtaining the required boosting duty ratio with given operating condition. Point A represents the crossing point of C_2 and C_3 as shown in Fig. 7

$${R_3}^2 = {R_2}^2 + (O_{3x} - O_{2x})^2 - 2R_2\,(O_{3x} - O_{2x})\cos(\omega D_b T_s) \tag{17}$$

$$D_b = \frac{1}{\omega T_s}\cos^{-1}\left[\frac{{R_2}^2 - {R_3}^2 + {V_o}^2}{2R_2V_o}\right]. \tag{18}$$

From (18), it can be noted that D_b is expressed by the operating conditions since ω, R_2, and R_3 are all expressed by the operating conditions in above-mentioned analysis. It can be noted that D_b can be obtained although $< v_{Cr} >$ is still unknown, since $(O_{3x} - O_{2x})$ cancels out $< v_{Cr} >$ in (17).

C. *Voltage Stresses on Devices*

The average output voltage of the full bridge inverter becomes zero since the duty ratio of the primary side switches is 0.5. Also, the average voltage across L_m is also zero according to the volt-second balance condition concluding that the average voltage on C_b is zero. Therefore, the maximum voltage on C_b can be obtained easily by $PT_s/8V_{\text{in}}C_b$.

Applying the volt-second balance condition to L_m can lead to $< v_{Cr} >$. It is assumed that the voltage across L_m becomes $< v_{Cr} > /n$ during 0–$(0.5 + D_b)T_s$ and $(-V_o + < v_{Cr} >)/n$ during $(0.5 + D_b)T_s$–T_s, respectively, as follows:

$$< v_{Cr} > = (0.5 - D_b)\,V_o. \tag{19}$$

From (19), it can be noted that $< v_{Cr} > = 0.5V_o$ when D_b is zero, which is in accordance with conventional series resonant converter without the boosting operation.

D. *Swing of i_{Lr} and Turn-off Current of the Boosting Switch*

In order to obtain the swing of i_{Lr}, it is required to obtain the positive and negative peaks. The positive peak iLr_pp can be easily obtained from the state trajectory analysis as follows:

$$i_{Lr\_pp} = |R_1|\,/Z. \tag{20}$$

The negative peak i_{Lr_np} can occur either at $t = t_2$ or during mode 3(t_2–t_3). In a deep boost region where D_b is large, O_3 locates outside of C_1, and the angle O_2O_3A becomes an acute angle and i_{Lr_np} becomes $R_2\sin(\omega D_b T_s)/Z$. On the other hand, in a shallow boost region where D_b is small, O_3 locates inside of C_1 and the angle O_2O_3A becomes an obtuse angle and i_{Lr_np} becomes R_3. Therefore, the angle O_2O_3A and i_{Lr_np} can be obtained the law of cosine as follows:

$$O_2O_3A = \cos^{-1}\left[\frac{{R_3}^2 + (O_{3x} - O_{2x})^2 - {R_2}^2}{2R_3\,(O_{3x} - O_{2x})}\right] \tag{21}$$

$$i_{Lr\_np} = \begin{cases} |R_2|\sin(\omega D_b T_s)\,/Z, & \text{if } O_2O_3A < 90\,(\text{deg}) \\ |R_3|\,/Z, & \text{if } O_2O_3A > 90\,(\text{deg}). \end{cases} \tag{22}$$

Finally, the current swing i_{Lr_swing} can be obtained as $i_{Lr\_\text{pp}} + i_{Lr\_np}$.

Also, it can be noted that the turn-off current of the boost switch i_{Lr_turnoff} is always $R_2\sin(\omega D_b T_s)/Z$ as follows:

$$i_{Lr\_\text{turnoff}} = R_2\sin(\omega D_b T_s)\,/Z. \tag{23}$$

E. Offset Current in the Transformer

General converters with asymmetric operation such as an asymmetric half-bridge converter have the offset current in the transformer. This offset current makes insufficient ZVS current for one main switch, and it causes a difficult ZVS condition to be achieved. However, there is no offset current in the transformer in the proposed converter, and ZVS condition is not affected by the transformer offset current.

From Fig. 2, the current on the magnetizing current i_{Lm}, the primary side current $i_{\rm pri}$, and the resonant inductor current i_{Lr} can be represented as follows:

$$i_{\rm pri} = i_{Lm} + \frac{N_s}{N_p} i_{Lr}. \quad (24)$$

At this point, i_{Lr} can be represented by i_{Cr1}–i_{Cr2}, and $i_{\rm pri}$ is equal to the current flowing through the blocking capacitor i_{Cb} as follows:

$$i_{\rm pri} = i_{Lm} + \frac{N_s}{N_p} i_{Lr} = i_{Lm} + \frac{N_s}{N_p}\left(i_{Cr1} - i_{Cr2}\right). \quad (25)$$

i_{Lm} can be presented by rearranging the above-mentioned equation as follows:

$$i_{Lm} = i_{Cb} + \frac{N_s}{N_p}\left(i_{Cr2} - i_{Cr1}\right). \quad (26)$$

By integrating the above-mentioned equation, the right-hand side becomes zero according to the charge balance of the capacitors, and it can be noted that the dc offset current in the transformer becomes zero in the proposed converter as follows:

$$\begin{aligned} < i_{Lm} >_{T_s} &= \frac{\int_0^{T_s} i_{Lm} dt}{T_s} \\ &= \frac{\int_0^{T_s} i_{Cb} dt + \frac{N_s}{N_p}\left(\int_0^{T_s} i_{Cr2} dt - \int_0^{T_s} i_{Cr1} dt\right)}{T_s} = 0. \quad (27) \end{aligned}$$

The proposed converter has no offset current in the transformer although it operates with asymmetrical current waveforms. Furthermore, since rms current of the transformer is also almost the same with the conventional converter, the transformer design can be the same with the conventional converter. Also, ZVS condition of the proposed converter is not affected by the transformer offset current. This is another powerful advantage of the proposed converter.

IV. COMPARISON WITH THE DESIGN RESULTS

To verify the effectiveness, the prototype converter has been designed and compared to conventional voltage doubler PWM resonant converter with 35–25 V input voltage and 380 V/300 W output for PV inverter. For the comparison, the conventional active voltage doubler rectifier in Fig. 1(d) has been selected. Table I presents the design results.

TABLE I
DESIGN RESULTS

Components	Design results
Resonant frequency	126 kHz
Q_1~Q_4	IPB030N08N3
Q_{sr}	SCT3080AL
D_r	C3D10060G
Transformer	RM14 N_p:N_s=4(AWG12):22(AWG17) L_m=13.9 µH L_r=48 µH n=5.5
C_r=C_{r1}+C_{r2}	33 nF
C_{in}	100 µF
C_b	66 µF
C_o	7 µF

Selecting switching frequency f_s can be done considering tradeoff between the size of magnetic components and losses. As f_s increases, the size of magnetic components can be decreased due to reduced flux swing. One the other hand, too high f_s results in high core loss in magnetic components and switching turn-OFF loss from $Q_{\rm sr}$. The resonant frequency f_r is selected as 126 kHz. The switching frequency has been selected as 135 kHz, so that the proposed converter has slightly higher switching frequency. By doing so, the proposed converter can assure ZVS of the primary side switches.

The resonant tank design is also critical to the performance of the boost mode series resonant converter. Considering the tradeoff among L_r loss, turn-OFF loss of $Q_{\rm sr}$, and overall conduction losses, L_r and C_r are selected as 48 μH and 33 nF, respectively. In order to maximize efficiency, the leakage inductance of the transformer with a separate winding is used for L_r instead of external inductor. Further design steps for this prototype are well described in our group's prior work with the same specification [23].

The prototype operates at the resonant point with $D_b = 0$ when the input voltage is the maximum as 35 V. Therefore, n is selected as 5.5 (22:4). As the input voltage decreases, D_b increases to regulate the output voltage.

A. Comparison of Voltage Conversion Ratio and $i_{Lr\_{\rm turnoff}}$

In order to obtain 380 V output voltage, the gain $(V_o/V_{\rm in})$ should vary from 10.86 to 15.2. Fig. 8 represents the gain versus D_b comparison with 60 and 300 W power conditions. The solid line represents the proposed modulation and the dotted line represents the conventional method, and the blue and red lines represent 300 and 60 W output conditions. As shown here, the proposed modulation requires higher D_b in the same operating condition.

This is because $< v_{Cr} >$ decreases as D_b increases in the proposed method, whereas $< v_{Cr} >$ remains constant as $V_o/2$ in the conventional method. The boosting current is built up by $nV_{\rm in} + < v_{Cr} >$ during the boosting period. Since the boosting slope decreases in the proposed method, required D_b increases in order to deliver the same amount of charges to the output capacitor. However, it should be noted that this does not affect

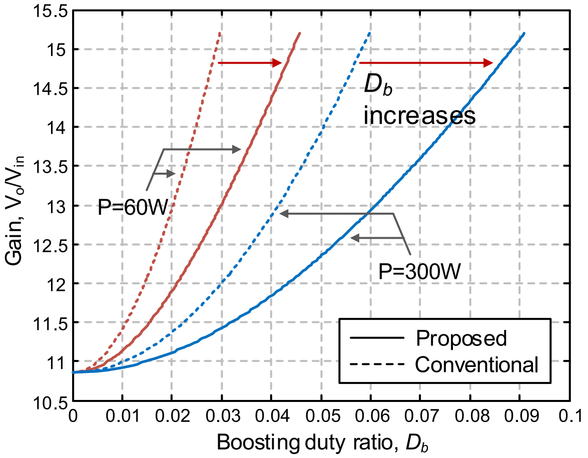

Fig. 8. Gain (V_o/nV_{in}) versus D_b comparison with 300 and 60 W power conditions.

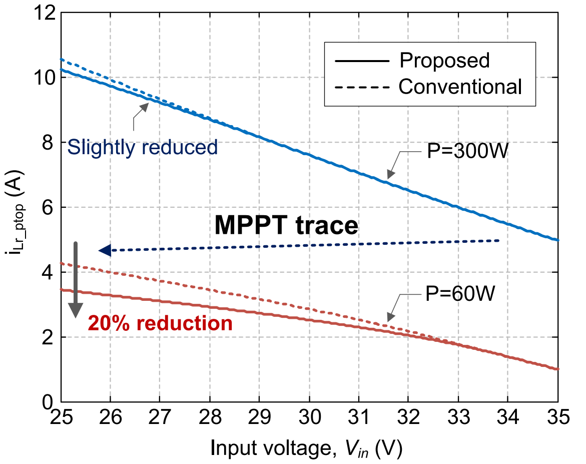

Fig. 10. Peak to peak value of i_{Lr} (i_{Lr_ptop}) versus V_{in} comparison with 300 and 60 W power conditions.

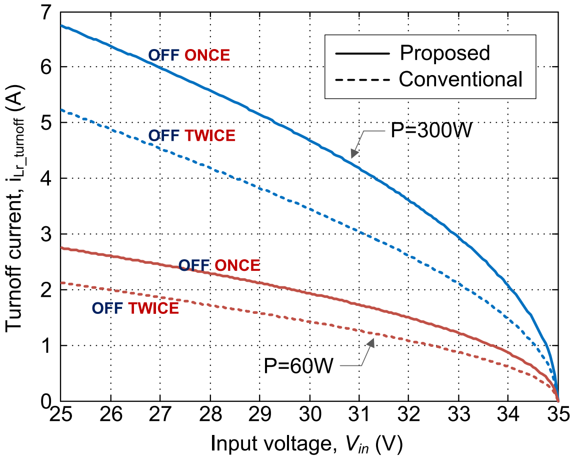

Fig. 9. Turn-OFF current of SR.

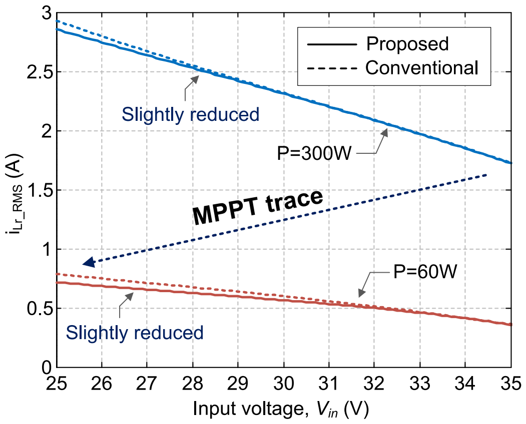

Fig. 11. RMS value of i_{Lr} (i_{Lr_RMS}) versus V_{in} comparison with 300 and 60 W power conditions.

the current swing in the circuit, because the total amount of charge delivered to the output side are the same in both cases. Also, the maximum D_b of the proposed method is as small as 0.1. Therefore, it is better to mention that the proposed modulation reduces the gain sensitivity to D_b.

Fig. 9 represents the turn-OFF current of the conventional active voltage douber rectifier and the proposed converter. In the boost region, the turn-OFF current can be interpreted as the peak current of resonant inductor, transformer winding, and the switches at the primary side. The peak current becomes slightly higher in the proposed converter. However, the proposed converter has only one switching turn OFF in a switching period, whereas the conventional has two.

B. RMS Current Comparison

Although the peak current becomes slightly higher in the proposed converter, the peak to peak of the resonant inductor i_{Lr_ptop} and the rms current of the resonant inductor i_{Lr_RMS} are reduced in the proposed converter as shown in Figs. 10 and 11.

From the time domain analysis provided in the previous chapter and key waveforms, rms value of i_{Lr} (i_{Lr_RMS}), which directly determines the conduction losses in the circuit, can be obtained as follows:

$$i_{Lr\_\text{RMS}} = \sqrt{\frac{1}{T_s}\int_0^{T_s} {i_{Lr}}^2 dt}. \tag{28}$$

Figs. 10 and 11 represent i_{Lr_ptop} and i_{Lr_RMS} versus V_{in} with 300 and 60 W power conditions. The solid line represents the proposed converter and the dotted line represents the conventional method, and the blue and red lines represent 300 and 60 W output conditions.

As shown here, when the input voltage is 35 V, the peak to peak values are the same in both cases due to the resonant operation. However, as the input voltage decreases, converter operates in a deeper boost region and i_{Lr_ptop} of the proposed modulation decreases due to the forced resonant operation. Especially, in 60 W condition, i_{Lr_ptop} reduced by 20%. In Fig. 11, it can be noted that the proposed converter has a reduced rms current and the conduction losses in all operating conditions. As mentioned before, this is because the proposed converter has a forced

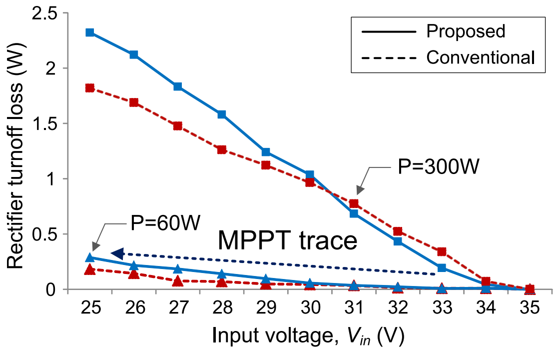

Fig. 12. Active switch turn-OFF loss comparison.

half resonant operation resulting in a reduced current swing in the circuit. At this point, as depicted by the navy dotted line in Figs. 10 and 11, it should be noted that maximum power point tracking (MPPT) operating point moves from the maximum input voltage/power to a minimum V_{in}/P condition, as the input voltage decreases with weaker sunlight. For these reasons, the proposed method will show reduced conduction loss in low input voltage/weak sunlight conditions so that the advantage of the proposed method can be maximized with PV applications.

C. Active Rectifier Turn-off Loss Comparison

Based on i_{Lr_turnoff} and LTspice pulse test, the turn-off losses are compared as shown in Fig. 12. It is shown that the proposed converter has a similar turn-OFF loss compared to the conventional modulation. In some region, the proposed converter shows a lower SR turn-OFF loss than the conventional converter, and in the other region the conventional converter shows a lower SR turn off loss. Considering MPPT trace in the figure, it can be noted that SR turn-OFF losses in both converters are almost the same each other the difference is less than 0.1 W. This is also because only one SR turn OFF in a switching period occurs in the proposed converter, whereas two turn-OFF actions occur in the conventional converter. Although the proposed converter has a higher turn-OFF current, the total turn-OFF loss is almost the same due to reduced number of switching actions.

D. Active Rectifier Turn-on Loss Comparison

Finally, the most powerful advantage of the proposed converter is ZVS operation in the voltage doubler PWM resonant converter. In the proposed converter, there is no turn-ON loss from any switching devices because it operates as a general SR. On the other hand, in the conventional converter, two large hard switching turn-ON actions occur in a switching period in all boost mode operation. The conventional converter can have ZVS operation of SR only when the converter operates at the resonant point. Although the conventional converter has ZCS turn-ON, the whole energy stored in the switches is dissipated and the switching turn-ON loss is substantial. The switching loss in the conventional one can be obtained as follows:

$$P_{\text{sw\_on\_conv}} = 2E_{\text{Coss}} f_s \qquad (29)$$

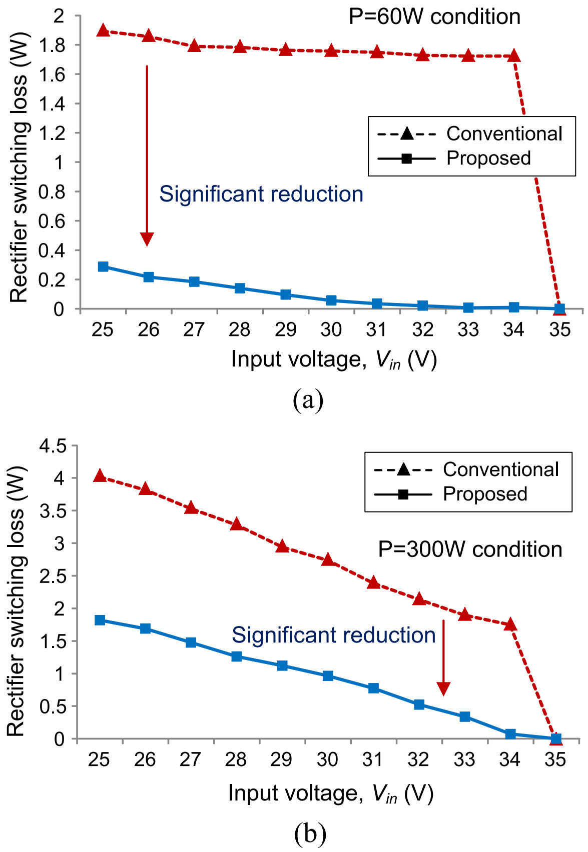

(a)

(b)

Fig. 13. Total rectifier switching loss comparison. (a) In 60 W. (b) In 300 W output conditions.

where E_{Coss} represents the energy stored in the output capacitor of the switch. From SCT3080AL datasheet, the switching turn-ON loss from SR in the conventional converter becomes $2(6.5\ \mu\text{J})(135\ \text{kHz}) = 1.76$ W, which means 0.6% loss in 300 W condition and even 3% loss in 60 W condition. Therefore, the proposed converter reduces the total switching loss significantly as shown in Fig. 13.

E. Conceptual Comparison With Other Conventional Works

Table II represents conceptual comparison of active rectifiers for PWM resonant converters. As shown here, the advantage of the proposed modulation can be interpreted as follows.

1) The proposed modulation can achieve the minimized number of switch component, since it requires only one boosting operation in a switching period. In order to improve the efficiency further, the rectifier diode can be replaced with the synchronous rectifier.

However, the proposed modulation is competitive in that it can be implemented only one switch and rectifier diode.

2) The proposed modulation can achieve ZVS in all switches. Because Q_{sr} is turned ON like a synchronous rectifier, there is no capacitive turn-ON loss. It should be noted that conventional active voltage doubler rectifier suffers from hard switching loss, resulting in an abrupt efficiency decrease in the boost region. It is the first method achieving ZVS based on voltage doubler rectifier.

TABLE II
CONCEPTUAL COMPARISON OF ACTIVE RECTIFIERS FOR PWM RESONANT CONVERTERS

Concepts	Bidirectional switch method [16]–[18]	Phase shifted modulation [19]	Sym. extended modulation [20]–[22]	Double pulse method [23]–[26]	Proposed
Rectifier structure	Voltage doubler	Full bridge	Full bridge	Voltage doubler	Voltage doubler
# of switches	**2**	**2**	**2**	**2**	**1**
# of diodes	**2**	**2**	**2**	**0**	**1**
ZVS	**X**	**O**	**O**	**X**	**O**

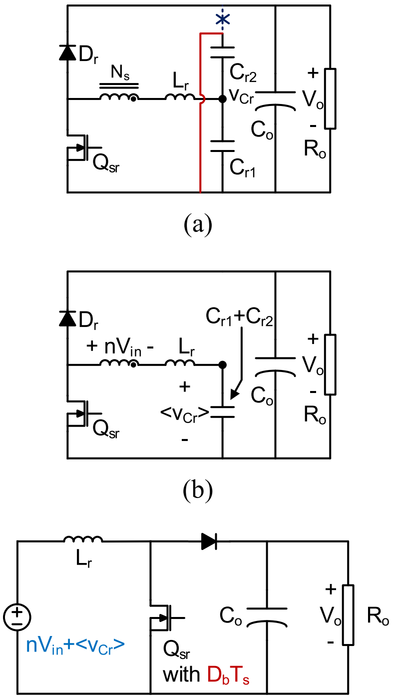

(a)

(b)

(c)

Fig. 14. Derivation of the small signal equivalent boost converter. (a) Cutting C_{r2}. (b) Merging C_{r1} and C_{r2} (electrically equivalent). (c) Merging voltage sources.

For these reasons, the proposed modulation shows the lowest number when we add all the number of semiconductor devices and turn-ON/turn-OFF losses as shown in Table II.

V. CONTROL TO OUTPUT TRANSFER FUNCTION

In order to analyze the control of the proposed converter, the control to output transfer function should be derived. The control to output transfer function of the proposed converter can be obtained from a simplified boost converter in discontinuous conduction mode (DCM). To derive the small signal equivalent boost converter intuitively, it is required to modify the secondary side of the proposed converter. The first step is to cut C_{r2} and merge it with C_{r1} as shown in Fig. 14(a) and (b). At this point, the circuit shown in Fig. 14(b) is electrically equivalent with Fig. 14(a) in terms of the steady state and small signal analysis. It can be easily known when the circuit in Fig. 14(b) is connected to the primary side of the converter. $C_{r1} + C_{r2}$ in the circuit in Fig. 14(b) will be charged during 0–$0.5T_s$, and will build i_{Lr} during $0.5T_s$–$(0.5 + D_b)T_s$, and i_{Lr} will be delivered during the remained switching period. At the last step, by assuming that i_{Lr} waveform is triangle, the secondary side of the transformer and $C_{r1} + C_{r2}$ can be regarded as the voltage sources. By rearranging the circuit, the small signal equivalent boost converter of the proposed converter can be obtained as shown in Fig. 14(c). Derivation of control to output transfer function of DCM boost converter is omitted in this paper.

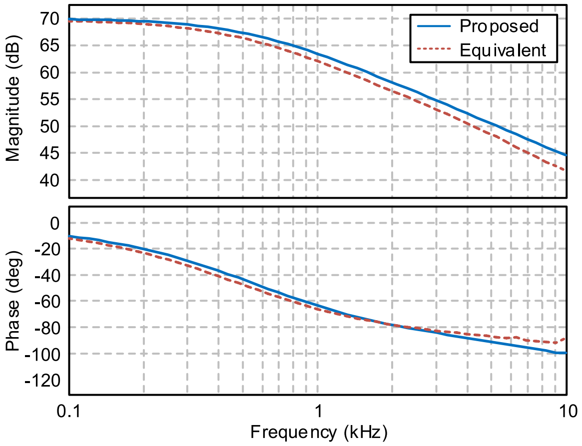

Fig. 15. Control to output transfer function of the proposed and the small signal equivalent boost converters at 29 V input and 90 W output condition.

Fig. 15 represents the control to output transfer function (D_b to V_o) of the proposed and the small signal equivalent boost converters at 29 V input and 90 W output condition obtained by PSIM ACsweep. It can be noted that the small signal transfer function of the proposed converter can be estimated by the equivalent circuit with a high accuracy.

VI. EXPERIMENTAL RESULTS

Fig. 16 represents the prototype converter. Fig. 17 represents key waveforms of the proposed converter in 30 V input voltage and 300 W output conditions. As designed in the previous chapter, the switching frequency (135 kHz) is slightly higher than the resonant frequency (126 kHz). It can be seen that the proposed

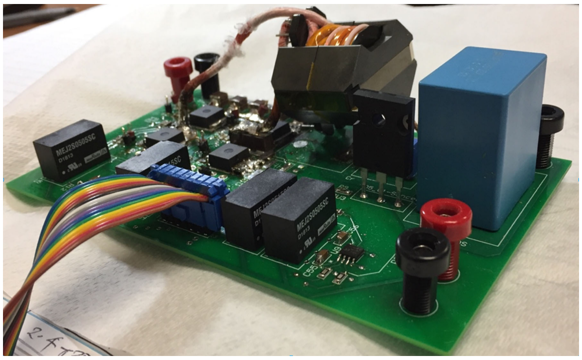

Fig. 16. Prototype converter.

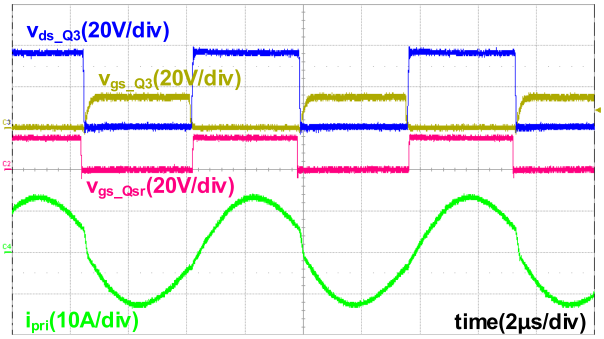

Fig. 17. Key waveforms in 35 V input 300 W output conditions.

converter operates near the resonant point so that the efficiency becomes the maximum at this point.

Figs. 18 and 19, respectively, represent key waveforms of the proposed converter in a boost mode at 32 and 25 V input voltage and different output conditions. During a half switching period, $i_{\rm pri}$ is a resonant waveform so that one turn-OFF loss can be eliminated.

Fig. 20 represents ZVS waveforms of the proposed converter in 29 V input voltage and 150 W output condition. It can be seen that the proposed converter achieves ZVS for all switching components. As mentioned before, this is a powerful advantage of the proposed modulation compared to other voltage doubler based conventional works.

Table III represents the PV panel maximum power points example according to the irradiance. Fig. 21(a) represents the efficiency of the prototype converter in various input and output conditions. Since PV panel provides less than 100 W maximum power when the sunlight is weak, the efficiency is measured up to 150 W in the case of 29 V/25 V input voltage condition. As shown here, the proposed converter achieves a high efficiency in a wide input voltage conditions. The efficiency becomes maximum when $V_{\rm in} = 35$ V due to the resonant operation. The overall efficiency drops as the input voltage decreases. The red dotted line represents the expected MPPT trace as the irradiance becomes weaker. According to the trace, the efficiency drops by just 1.5% according to the expected MPPT trace. The most powerful advantage of the proposed modulation is a significantly

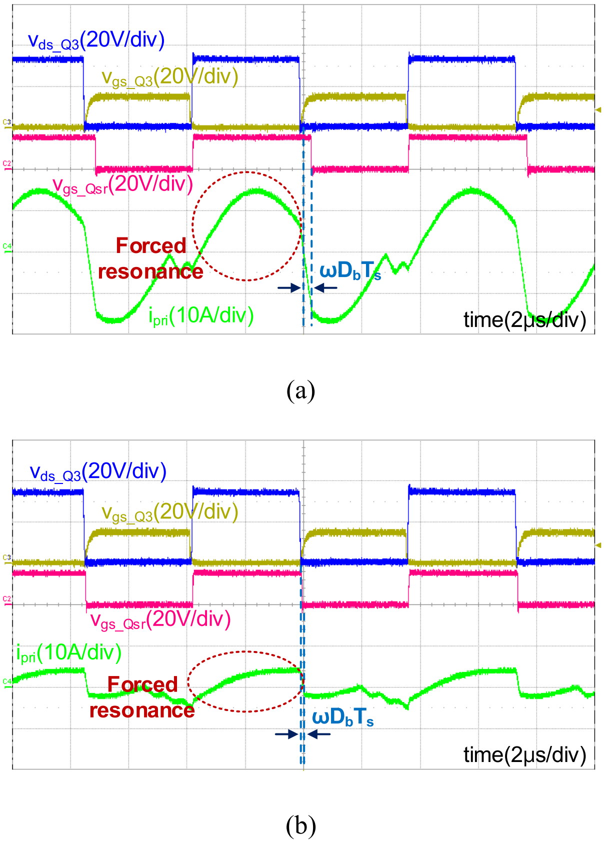

Fig. 18. Key waveforms in 32 V input. (a) 300 W. (b) 150 W output conditions.

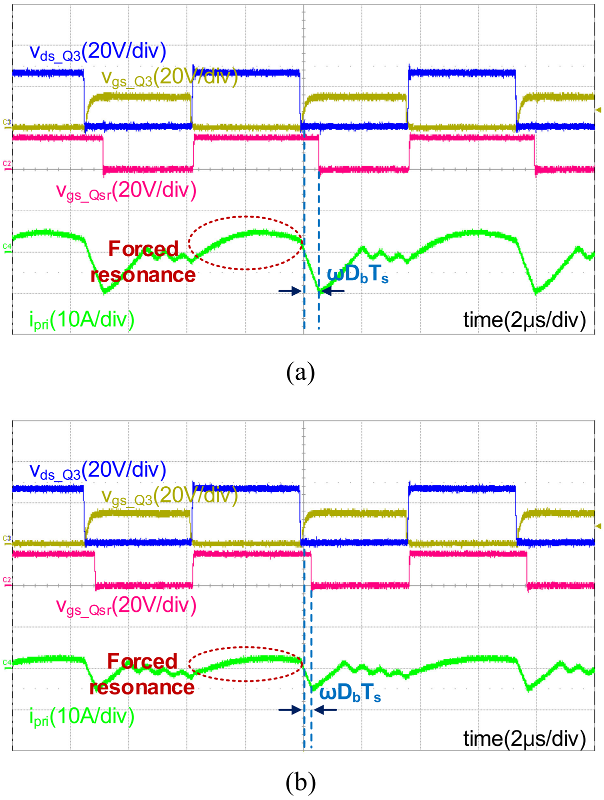

Fig. 19. Key waveforms in 25 V input. (a) 150 W. (b) 60 W output conditions.

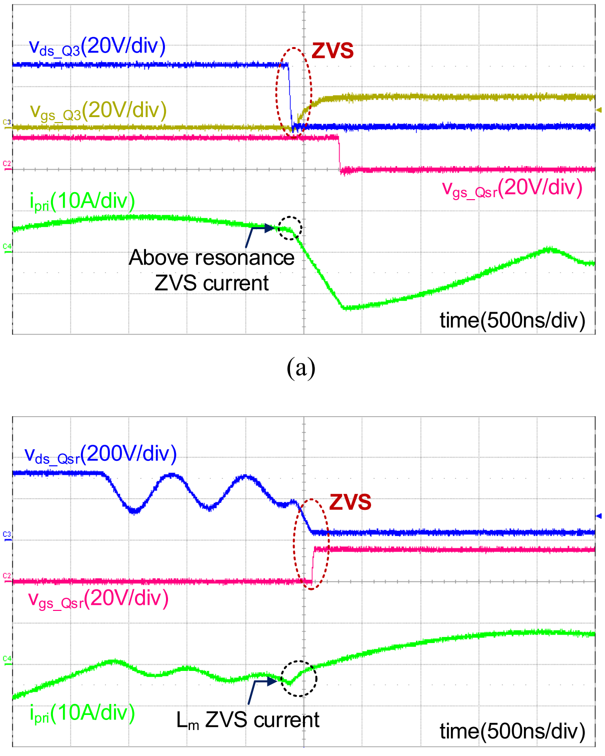

(a)

(b)

Fig. 20. ZVS waveforms in 25 V input and 150 W output condition. (a) Q_3. (b) $Q_{\rm sr}$.

TABLE III
PV PANEL MAXIMUM POWER POINTS EXAMPLE ACCORDING TO THE IRRADIANCE

Irradiance	Maximum power	Voltage at the maximum power
1000 W/m^2	300 W	35 V
530 W/m^2	160 W	32 V
300 W/m^2	90 W	29 V
150 W/m^2	45 W	25 V

improved efficiency when the input voltage is low. Fig. 21(b) represents the comparison of MPPT trace between proposed work and the conventional active voltage doubler rectifier [23]. As shown here, the proposed work shows significantly improved efficiency. For example, the efficiency is improved by up to 3% when the output power is 40 W. The efficiency is even higher at the maximum output power condition since it is designed with integrated resonant inductor. As analyzed in the previous chapters, the proposed work shows a higher efficiency when the power decreases, due to the forced resonant operation, reduced flux swing, and ZVS operation of all switching devices.

Fig. 22 represents comparative loss analysis between the proposed converter and the PWM resonant converter with conventional active voltage doubler at 29 V input and 90 W output condition. From Fig. 22, it can be seen that the elimination of turn-ON loss in the synchronous rectifier made the proposed converter have a superior efficiency. Although the proposed converter has asymmetric current stress on the primary side switches, conduction losses from them were less than 0.2 W, so the unbalance between them is negligible. Specific explanation for this loss analysis is provided in the previous section.

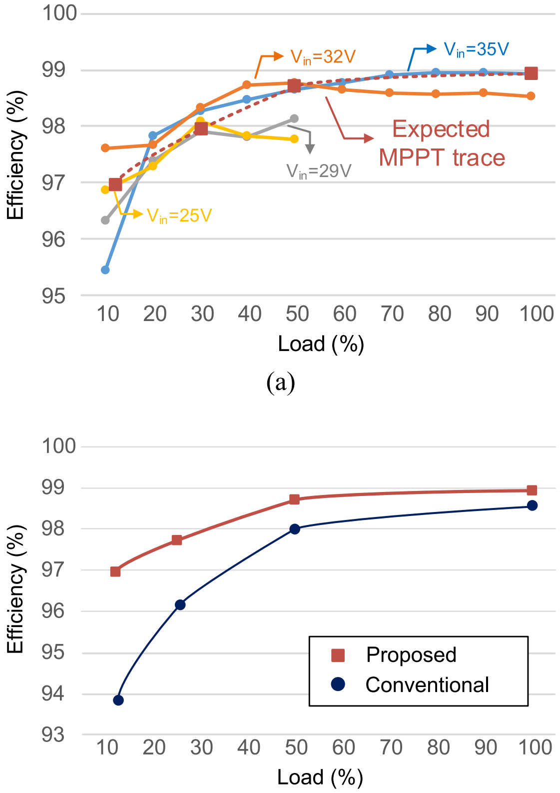

(a)

(b)

Fig. 21. (a) Efficiency of the prototype converter. (b) Expected MPPT trace comparison with conventional active voltage doubler rectifier.

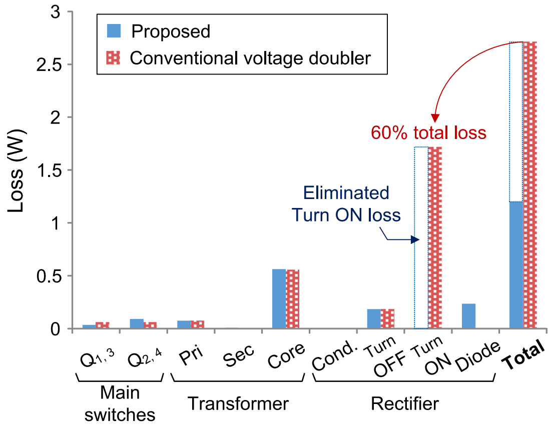

Fig. 22. Comparative loss analysis at 29 V input and 90 W output condition.

VII. CONCLUSION

In this paper, a new converter with a novel asymmetrical modulation is proposed and verified. The strong point of the proposed converter is that it eliminates hard switching turn-ON losses from the rectifier, while maintaining the minimized number of components. Although the proposed converter adopts an asymmetric modulation, the offset current on the transformer becomes zero inherently. Furthermore, a "forced half resonance" operation of the proposed converter keeps rms current stresses at the same level as conventional converter although it has a higher peak current. Accordingly, the proposed converter achieves a superior efficiency with the minimum number of components.

REFERENCES

[1] Solar Power Europe, Global Market Outlook 2018–2022, 2018. [Online]. Available: http://www.solarpowereurope.org/global-market-outlook-2018-2022/

[2] Department of Energy, Photovoltaics Research and Development, 2012. [Online]. Available: https://www.pv-tech.org/news/report_solar_fastest_groving_renewable_in_us_to_2040

[3] P. V. Tech, Report: Solar Fastest Growing Renewable in US to 2040, 2012. [Online]. Available: http://www.pv-tech.org/news/report_solar_fastest_growing_renewable_in_us_ to_ 2040/

[4] K.-C. Tseng and C.-C. Huang, "High step-up high-efficiency interleaved converter with voltage multiplier module for renewable energy system," *IEEE Trans. Ind. Electron.*, vol. 61, no. 3, pp. 1311–1319, Mar. 2014.

[5] F. Evran and M. T. Aydemir, "Isolated high step-up DC-DC converter with low voltage stress," *IEEE Trans. Power Electron.*, vol. 29, no. 7, pp. 3591–3603, Jul. 2014.

[6] G. Wu, X. Ruan, and Z. Ye, "Nonisolated high step-up DC-DC converter adopting switched-capacitor cell," *IEEE Trans. Ind. Electron.*, vol. 62, no. 1, pp. 383–393, Jan. 2016.

[7] P. Saadat and K. Abbaszadeh, "A single-switch high step-up DC-DC converter based on quadratic boost," *IEEE Trans. Ind. Electron.*, vol. 63, no. 12, pp. 7733–7742, Dec. 2016.

[8] M. Forouzesh, Y. Shen, K. Yari, Y. P. Siwakoti, and F. Blaabjerg, "High-efficiency high step-up DC-DC converter with dual coupled inductors for grid-connected photovoltaic systems," *IEEE Trans. Power Electron.*, vol. 33, no. 7, pp. 5967–5982, Jul. 2018.

[9] G. Wu, X. Ruan, and Z. Ye, "High step-up DC-DC converter based on switched capacitor and coupled inductor," *IEEE Trans. Ind. Electron.*, vol. 65, no. 5, pp. 5572–5579, Jul. 2018.

[10] L. Schmitz, D. C. Martins, and R. F. Coelho, "High step-up nonisolated ZVS/ZCS DC-DC converter for photovoltaic thin-film module applications," *IEEE J. Emerg. Sel. Topics Power Electron.*, vol. 7, no. 1, pp. 565–575, Mar. 2019.

[11] A. Andrade, L. Schuch, and M. Martins, "Analysis and design of high-efficiency hybrid high step-up DC-DC converter for distributed PV generation systems," *IEEE Trans. Ind. Electron.*, vol. 66, no. 5, pp. 3860–3868, May 2019.

[12] Y. Gu, Y. Chen, B. Zhang, D. Qiu, and F. Xie, "High step-up DC-DC converter with active switched LC-network for photovoltaic systems," *IEEE Trans. Energy Convers.*, vol. 34, no. 1, pp. 321–329, Mar. 2019.

[13] X. Sun, X. Li, B. Wang, and X. Guo, "Dual-bridge LLC resonant converter with fixed-frequency PWM control for wide input applications," *IEEE Trans. Power Electron.*, vol. 32, no. 1, pp. 69–80, Jan. 2017.

[14] H. Wang and Z. Li, "A PWM LLC type resonant converter adapted to wide output range in PEV charging applications," *IEEE Trans. Power Electron.*, vol. 33, no. 5, pp. 3791–3801, May 2018.

[15] X. Gao, H. Wu, and Y. Xing, "A multioutput LLC resonant converter with semi-active rectifiers," *IEEE J. Emerg. Sel. Topics Power Electron.*, vol. 5, no. 4, pp. 1819–1827, Dec. 2017.

[16] T. LaBella and J.-S. Lai, "A hybrid resonant converter utilizing a bidirectional GaN AC switch for high-efficiency PV applications," *IEEE Trans. Ind. Appl.*, vol. 50, no. 5, pp. 3468–3475, May 2014.

[17] T. LaBella and J.-S. Lai, "A hybrid resonant converter utilizing a bidirectional GaN AC switch for high-efficiency PV applications," in *Proc. IEEE Appl. Power Electron. Conf. Expo.*, 2014, pp. 1–8.

[18] T. LaBella, W. Yu, J.-S. Lai, M. Senesky, and D. Anderson, "A bidirectional-switch-based wide-input range high-efficiency isolated resonant converter for photovolaic applications," *IEEE Trans. Power Eletron.*, vol. 29, no. 7, pp. 3473–3484, Jul. 2014.

[19] J.-W. Kim and G.-W. Moon, "A new LLC series resonant converter with a narrow switching frequency variation and reduced conduction losses," *IEEE Trans. Power Electron.*, vol. 29, no. 8, pp. 4278–4287, Aug. 2014.

[20] X. Zhao, L. Zhang, R. Born, and J.-S. Lai, "A high-efficiency hybrid resonant converter with wide-input regulation for photovoltaic applications," *IEEE Trans. Ind. Electron.*, vol. 64, no. 5, pp. 3684–3694, May 2017.

[21] X. Zhao, L. Zhang, R. Born, and J.-S. Lai, "Output capacitance effect on the voltage gain in the high step-up series resonant converter," in *Proc. IEEE 2nd Int. Future Energy Electron. Conf.*, 2015, pp. 1–5.

[22] X. Zhao, L. Zhang, Q. Ma, and J.-S. Lai, "Modeling and control of a wide-input hybrid resonant microconverter for photovoltaic applications," in *Proc. Asian Conf. Energy, Power Transp. Electrific.*, 2016, pp. 1–6.

[23] X. Zhao, C.-W. Chen, and J.-S. Lai, "A high-efficiency active-boost-rectifier-based converter with a novel double-pulse duty cycle modulation for PV to DC microgrid applications," *IEEE Trans. Ind. Electron.*, to be published, doi: 10.1109/TPEL.2018.2878225.

[24] X. Zhao, C.-W. Chen, and J.-S. Lai, "A GaN-based high-efficiency solar optimizer with reduced number of power devices," in *Proc. IEEE Energy Convers. Congr. Expo.*, 2018, pp. 6202–6206.

[25] H. Seok, B. Han, B.-H. Kwon, and M. Kim, "High step-up resonant DC-DC converter with ripple-free input current for renewable energy systems," *IEEE Trans. Ind. Electron.*, vol. 65, no. 11, pp. 8543–8552, May 2018.

[26] S. Kim, B. Kim, B.-H. Kwon, and M. Kim, "An active voltage-doubler rectifier based hybrid resonant DC/DC converter for wide-input-range thermoelectric power generation," *IEEE Trans. Power Electron.*, vol. 33, no. 11, pp. 9470–9481, Nov. 2018.

[27] R. Beiranvand, B. Rashidian, M. R. Zolghadri, and S. M. H. Alavi, "A design procedure for optimizing the LLC resonant converter as a wide output range voltage source," *IEEE Trans. Power Electron.*, vol. 27, no. 8, pp. 3749–3763, Aug. 2012.

[28] R. Beiranvand, B. Rashidian, M. R. Zolghadri, and S. M. H. Alavi, "Using LLC resonant converter for designing wide-range voltage source," *IEEE Trans. Ind. Electron.*, vol. 58, no. 5, pp. 1746–1756, May 2011.

[29] F. Musavi, M. Craciun, D. S. Gautam, W. Eberle, and W. G. Dunford, "An LLC resonant DC–DC converter for wide output voltage range battery charging applications," *IEEE Trans. Power Electron.*, vol. 28, no. 12, pp. 5437–5445, Dec. 2013.

[30] H. Hu, X. Fang, F. Chen, Z. J. Shen, and I. Batarseh, "A modified high efficiency LLC converter with two transformers for wide input-voltage range applications," *IEEE Trans. Power Electron.*, vol. 28, no. 4, pp. 1946–1960, Apr. 2013.

[31] J.-W. Kim, J.-P. Moon, and G.-W. Moon, "Duty-ratio-control-aided LLC converter for current balancing of two-channel LED driver," *IEEE Trans. Ind. Electron.*, vol. 64, no. 2, pp. 1178–1184, Feb. 2017.

[32] C.-O. Yeon, J.-W. Kim, M.-H. Park, I.-O. Lee, and G.-W. Moon, "Improving the light-load regulation capability of LLC series resonant converter using impedance analysis," *IEEE Trans. Power Electron.*, vol. 32, no. 9, pp. 7056–7067, Apr. 2013.

[33] D.-K. Kim, S. Moon, C.-O Yeon, and G.-W. Moon, "High-efficiency LLC resonant converter with high voltage gain using an auxiliary LC resonant circuit," *IEEE Trans. Power Electron.*, vol. 31, no. 10, pp. 6901–6909, Oct. 2016.

Jong-Woo Kim (S'13–M'16) received the B.S., M.S., and Ph.D. degrees in electrical engineering from the Korea Advanced Institute of Science and Technology, Daejeon, South Korea, in 2010, 2012, and 2016, respectively. From 2016 to 2019, he was a Research Assistant Professor and Postdoctoral Researcher with Virginia Tech, Blacksburg, VA, USA.

Since 2019, he has been a member of R&D Staff with the Power Electronics Laboratory, Delta Products Corporation, Research Triangle Park, NC, USA. He has authored/coauthored 19 journal articles and more than 20 technical papers in conference proceedings. His research interests include high-efficiency power converters, high power density design with PCB winding transformer and wide-bandgap devices, and analog/digital control.

Moo-Hyun Park (S'16) received the B.S. and M.S. degrees in electrical engineering in 2015 and 2017, respectively, from Korea Advanced Institute of Science and Technology, Daejeon, South Korea, where he is currently working toward the Ph.D. degree.

His main research interests include following areas of power electronics—dc/dc converters, ac/dc converters, soft-switching technique, and digital control of power converters.

Jung-Kyu Han (S'16) was born in South Korea, in 1991. He received the B.S. and M.S. degrees in electrical engineering in 2014 and 2016, respectively, from the Korea Advanced Institute of Science and Technology (KAIST), Daejeon, South Korea, where he is currently working toward the Ph.D. degree.

His research interests include dc–dc converters, power-factor-correction ac/dc converters, digital control, server power system, and on-board charger for EV.

Moonhyun Lee (S'18) received the B.S. and M.S. degrees in electrical and computer engineering from Seoul National University, Seoul, South Korea, in 2014 and 2016, respectively. He is currently working toward the Ph.D. degree at Virginia Tech, Blacksburg, VA, USA.

His research interests include control of dc–dc converters, power factor correction rectifier, and multilevel inverters.

Jih-Sheng (Jason) Lai (S'85–M'89–SM'93–F'07–LF'19) received M.S. and Ph.D. degrees in electrical engineering from the University of Tennessee, Knoxville, TN, USA, in 1985 and 1989, respectively.

In 1989, he joined the Electric Power Research Institute (EPRI) Power Electronics Applications Center (PEAC), where he managed EPRI-sponsored power electronics research projects. In 1993, he then joined the Oak Ridge National Laboratory as Power Electronics Lead Scientist, where he initiated a high power electronics program and developed several novel high power converters including multilevel converters and soft-switching inverters. In 1996, he joined Virginia Polytechnic Institute and State University. He is currently the James S. Tucker Professor with the Electrical and Computer Engineering Department and Director of Future Energy Electronics Center. He authored or coauthored more than 430 refereed technical papers, one book chapter, two books, and 27 patents. His main research areas are in high efficiency power electronics conversions for high power and energy applications.

Dr. Lai was the recipient of the Technical Achievement Award in Lockheed Martin Award Night, two Journal Paper awards, and 12 Best Paper awards from IEEE sponsored conferences. He was also the recipient of 2016 IEEE IAS Gerald Kliman Innovator Award. He led the student teams to win the Top Three Finalist in Google Little Box Challenge in 2016, Grand Prize Award from International Future Energy Challenge (IFEC) in 2011, and Grand Prize Award from Texas Instruments Engibous Analog Design Competition in 2009. He is the Founding Chairs of 2001 IEEE IFEC and 2016 IEEE ACEPT, General Chairs of IEEE COMPEL-2000, IEEE APEC 2005, IEEE SPEC-2018, and IEEE IFEEC-2019 conferences.